Microwave Imaging Algorithm Based on Waveform Reconstruction for Microwave Ablation Treatment

Kazuki Kanazawa, Kazuki Noritake, Yuriko Takaishi, and Shouhei Kidera, *Member, IEEE*

***Abstract*—Microwave ablation (MWA), intended for treating malignant tissues, must be monitored in real time for effective treatment and patient safety. In this article, we propose an imaging algorithm that corrects for errors that typically arise at the boundary of an ablation image when the tissue's dielectric properties are a little affected by ablation. Conventional imaging algorithms exploit the difference in the propagation time of signals through nonablated and ablated tissues in order to monitor the dimensions of an ablation in real time, but this time difference does not account for the drop in conductivity that occurs as the tissue dries out, causing nonnegligible errors, particular in lower ablation impact case. In order to address this problem, the method that we propose incorporates waveform reconstruction in accounting for the change in conductivity. We test this method with 2-D and 3-D numerical simulations of microwave signals propagating in two computational phantoms of breast tissue with different densities. Simulations with differently affected tissues show that the proposed method improves upon the accuracy of conventional MWA monitoring techniques, with an acceptable increase in the computation time.**

***Index Terms*—Microwave ablation (MWA), microwave-based ablation dimension monitoring, time difference of arrival (TDOA), waveform reconstruction.**

I. Introduction

MICROWAVE ablation (MWA) is one of the most promising tools considering a minimally invasive cancer treatment. Microwave-frequency radiation heats up cells more quickly than lower radio frequency radiation can [1]. Several studies have demonstrated that MWA is an effective clinical tool for treating liver tumors [2]. It can also be applied in the treatment of other types of cancer, such as kidney or breast tumors. MWA treatment for breast tumors can significantly reduce the physical and mental burdens on patients by eliminating the need for the large-scale removal of breast tissue. For a safe and effective ablation of malignant tumors without damaging healthy tissues, MWA needs to be implemented alongside appropriate imaging modality tools. For such imaging needs, magnetic resonance imaging (MRI) and ultrasound-based methods have been developed and tested. However, MRI requires large-scale and expensive equipment, as well as consideration of the effect of heating contrast agents [3]. Ultrasound imaging equipment is less expensive and more compact than the equipment for MRI, but the microbubbles caused by ablation can contaminate the contrast image [4].

Microwave-based imaging is a promising alternative in terms of cost, compactness, and compatibility with MWA equipment. However, the dielectric properties of tissues at microwave frequencies are sensitive to the temperature and the physiological state of the tissue [5]. Similarly, ablated tissues exhibit a large drop in complex permittivity for microwave radiation [6]. Based on these features, the dimensions of the ablated tissue can be monitored by measuring the forward-scattered components received at an external antenna from an interstitial MWA source and by processing this signal with an appropriate algorithm. MWA in the liver tissue is monitored with a range of tomographic algorithms, which are only effective if the tissue is relatively homogeneous, as the liver is [7] and [8]. However, these methods do not return images in real time and cannot produce images with a heterogeneous background, as we found in the breast. Moghaddam [9], [10] and coworkers proposed an inverse scattering-based imaging method exploiting time differential scattered data; however, it was based on an iterative approach using a forward solver, for example, the distorted Born iterative method. This means that the imaging accuracy is largely dependent on the initial guess of the dielectric map, and it requires the forward solver, which is time consuming especially for the 3-D problem, and needs to be given for accurate information of dielectric property, including antennas and other fixtures.

As a promising approach achieving a real-time, accurate, and noise-robust ablation zone imaging with much more simple process, the time-difference-of-arrival- (TDOA)-based imaging algorithm has been developed, which exploits the TDOA of forward-scattered signals before treatment and at a specific time during ablation [11]. This algorithm requires minimal *a priori* knowledge: only an estimate of the relative permittivity of the tissue in the local treatment zone before the ablation begins and an estimate of the change in relative permittivity of that tissue due to ablation. 2-D and 3-D finite-difference-time-domain- (FDTD)-based tests have shown that this method simultaneously accomplishes real-time, noise-robust, accurate imaging of the ablation zone, even when imaging highly heterogeneous breast tissues. However, this algorithm suffers from nonnegligible inaccuracies for boundary extraction, especially if ablation has a relatively low impact on the dielectric constant of the treated tissue.

Manuscript received November 17, 2019; revised January 20, 2020; accepted February 3, 2020. Date of publication February 14, 2020; date of current version July 7, 2020. This work was supported in part by the MIC/SCOPE under Grant 162103102 and in part by the Strategic Information and Communications Research and Development Promotion Program (SCOPE) promoted by the Japanese Ministry of Internal Affairs and Communications under Grant 162103102. *(Corresponding author: Shouhei Kidera.)*

The authors are with the Graduate School of Informatics and Engineering, University of Electro-Communications, Tokyo 1828585, Japan (e-mail: kidera@ee.uec.ac.jp).

Color versions of one or more of the figures in this article are available online at http://ieeexplore.ieee.org.

Digital Object Identifier 10.1109/TAP.2020.2972633

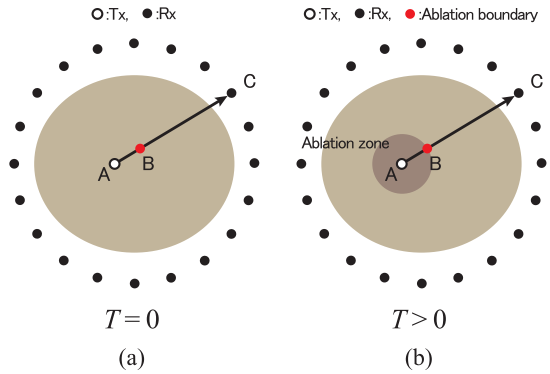

Fig. 1. Data acquisition configuration. (a) Preablation ($T = 0$). (b) During ablation ($T > 0$).

In order to address this problem at the boundaries of TDOA-derived images, in this article, we introduce an imaging method based on waveform reconstruction, which we have recently proposed [12]. In this method, the forward-scattered signal during ablation is reconstructed from a signal measured before treatment. Using a simple forward propagation model, the algorithm considers drops in both the real and the imaginary parts of the tissue's complex permittivity as the impact of ablation. This method retains the most significant advantage of the TDOA-based algorithm, in that it requires only estimates of the average relative permittivity and conductivity of the tissue near the MWA antenna before and during treatment, which can be inferred from temperature monitoring using a growing database of tissue measurements. Note that, since the proposed method is based on simple propagation model, it is especially useful in the early stage in the ablation process, where a lower impact on dielectric property and smaller size of ablation should be considered. The 2-D and 3-D FDTD-based investigations, including statistical analysis of different simulated ablation treatments, demonstrate that our proposed method delivers more accurate estimates of the ablation zone than the previously reported TDOA algorithm does.

II. Observation Model

Fig. 1 shows the data acquisition configuration of the MWA monitoring strategy. The elapsed time of the ablation signal is denoted by T. A single transmitter (shown as a hollow black circle in Fig. 1) is inserted into the tumor, which would be located within the fibroglandular tissue, and several receivers are located around the breast (shown as solid black circles in Fig. 1). The location of the source is defined as $\boldsymbol{r}_{\rm A}$, and the location of a representative receiver is defined as $\boldsymbol{r}_{\rm C}$. The received microwave signals before ablation (at $T = 0$) and during ablation (at the nth temporal snapshot) are denoted by $s_0(\boldsymbol{r}_{\rm C}, t)$ and $s_n(\boldsymbol{r}_{\rm C}, t)$, respectively. The variable t denotes the signal-recording time.

III. Ablation Boundary Estimation Algorithm

A. TDOA-Based Method

As a real-time, noise-robust, accurate monitoring algorithm for the ablation zone, the TDOA-based algorithm has been developed [11], which exploits the time difference of propagation from the interstitial source to the receivers, caused by the relative permittivity drop. This section briefly describes this TDOA-based algorithm, for the sake of comparison with the proposed method. It exploits the well-studied physical finding that ablation leads to a decrease in the permittivity of tissues near the MWA probe, mainly due to dehydration. The lower relative permittivity of the ablation zone reduces the time delay from the source to the receiver. This difference in the time delay is exploited as follows. Let τ_0 and τ_n be the times that signals passing through preablated and during ablated tissues arrive at location C, respectively. Each time of arrival can be decomposed as follows:

$$\tau_0 = \tau_0^{\rm AB} + \tau_0^{\rm BC} \tag{1}$$
$$\tau_n = \tau_n^{\rm AB} + \tau_n^{\rm BC} \tag{2}$$

where $\tau^{\rm AB}$ and $\tau^{\rm BC}$ denote the transit times from $\boldsymbol{r}_{\rm A}$ (source location) to $\boldsymbol{r}_{\rm B}$ (ablation boundary point), and from $\boldsymbol{r}_{\rm B}$ to $\boldsymbol{r}_{\rm C}$ (receiver location), respectively, as marked in Fig. 1. We define $\epsilon_n^{\rm AB}$ as the dielectric constant of the tissue inside the ablation zone at the nth moment and $\epsilon_0^{\rm AB}$ as the dielectric constant of preablated tissue. In addition, $\tau_0^{\rm BC} \simeq \tau_n^{\rm BC}$ because the dielectric properties of the tissue between B and C do not change. The TDOA between preablated and during ablated tissue cases can then be approximated as follows:

$$\begin{aligned}\Delta\tau &\equiv \tau_0 - \tau_n \\ &\simeq (1 - \sqrt{\xi})\tau_0^{\rm AB}\end{aligned} \tag{3}$$

where $\xi = \epsilon_n^{\rm AB}/\epsilon_0^{\rm AB}$. From (3), we can estimate the distance from the source to a boundary point as follows:

$$\begin{aligned}R^{\rm AB} \equiv ||\boldsymbol{r}_{\rm A} - \boldsymbol{r}_{\rm B}|| &\simeq v_0\tau_0^{\rm AB} \\ &\simeq v_0\frac{\Delta\tau}{1-\sqrt{\xi}}\end{aligned} \tag{4}$$

where v_0 denotes the propagation velocity in the preablated medium. The ablation boundary point $\boldsymbol{r}_{\rm B}$ is then given by

$$\boldsymbol{r}_{\rm B} = R^{\rm AB}\boldsymbol{u} + \boldsymbol{r}_{\rm A} \tag{5}$$

where $\boldsymbol{u}$ denotes a unit vector pointing from $\boldsymbol{r}_{\rm A}$ to $\boldsymbol{r}_{\rm C}$. Note that $\Delta\tau$ can be estimated from the following cross correlation calculation:

$$\Delta\tau = \arg\max_{\tau}\,[s_0(\boldsymbol{r}_{\rm C}, t) \star s_n(\boldsymbol{r}_{\rm C}, t)]\,(\tau) \tag{6}$$

where $\star$ denotes the cross correlation operator. If the number of receivers is M, then M different boundary points $\boldsymbol{r}_{\rm B}$ can be located. This method notably only requires two pieces of information before imaging: 1) an estimate of the average signal velocity in the medium surrounding the source before the ablation begins and 2) an estimate of the ratio of the preablated tissue's dielectric constant to its ablated dielectric constant. While a number of tests have demonstrated that the above TDOA-based method is rapid enough for real-time ablation monitoring and is robust against noise, this algorithm does not consider the impact of the decrease in conductivity that tissue experience as they dry out. In addition, some tests have revealed that this method suffers from inaccuracies when the lower ablation impact, that is, ξ is close to 1.

B. Proposed Method

1) Imaging Principle: In order to address the inaccuracy in the lower impact of the ablation described in Section III-A, in this article, we introduce a waveform reconstruction-based imaging algorithm, where the frequency dependence in the propagating medium is compensated for by considering the conductivity drop in the estimation. This decrease in conductivity affects not only the amplitude of the forward-scattered signal but also the phase of the signal. Waveform reconstruction to recover this phase information could further improve the accuracy of ablation imaging.

Here, let $\boldsymbol{r}_\mathrm{B}$ as the ablation boundary point. Under the assumption that the same propagation model, used in the TDOA-based method, is valid and that signals propagate in a straight line, using the parameter R^{AB}, the preablated and during ablated signals in the angular-frequency domain can be expressed as

$$S_0(\boldsymbol{r}_\mathrm{C}, \omega; R^{\mathrm{AB}}) = G(\|\boldsymbol{r}_\mathrm{C} - \boldsymbol{r}_\mathrm{B}\|; k(\omega)) \times G(\|\boldsymbol{r}_\mathrm{B} - \boldsymbol{r}_\mathrm{A}\|; k_0(\omega)) S_{\mathrm{src}}(\boldsymbol{r}_\mathrm{A}, \omega) \quad (7)$$

$$S_n(\boldsymbol{r}_\mathrm{C}, \omega; R^{\mathrm{AB}}) = G(\|\boldsymbol{r}_\mathrm{C} - \boldsymbol{r}_\mathrm{B}\|; k(\omega)) \times G(\|\boldsymbol{r}_\mathrm{B} - \boldsymbol{r}_\mathrm{A}\|; k_n(\omega)) S_{\mathrm{src}}(\boldsymbol{r}_\mathrm{A}, \omega) \quad (8)$$

where $S_0(\boldsymbol{r}_\mathrm{C}, \omega; R^{\mathrm{AB}})$ and $S_n(\boldsymbol{r}_\mathrm{C}, \omega; R^{\mathrm{AB}})$ denote the signals received before and during ablation at the nth snapshot in the angular-frequency domain, respectively, and $S_{\mathrm{src}}(\boldsymbol{r}_\mathrm{A}, \omega)$ denotes the transmitted signal from the source located at $\boldsymbol{r}_\mathrm{A}$. $G(\|\boldsymbol{r}_\mathrm{B} - \boldsymbol{r}_\mathrm{C}\|; k(\omega))$ denotes the Green's function in propagating from $\boldsymbol{r}_\mathrm{C}$ to $\boldsymbol{r}_\mathrm{B}$ with the wavenumber $k(\omega)$. $G(\|\boldsymbol{r}_\mathrm{B} - \boldsymbol{r}_\mathrm{A}\|; k_n(\omega))$ and $G(\|\boldsymbol{r}_\mathrm{B} - \boldsymbol{r}_\mathrm{A}\|; k_n(\omega))$ also denote the Green's functions in propagating from $\boldsymbol{r}_\mathrm{B}$ to $\boldsymbol{r}_\mathrm{A}$ ($R^{\mathrm{AB}} \equiv \|\boldsymbol{r}_\mathrm{B} - \boldsymbol{r}_\mathrm{A}\|$) at the preablation and during ablation states, each wavenumber of which is expressed as $k_0(\omega)$ and $k_n(\omega)$, respectively. The wavenumber at the nth snapshot $k_n(\omega)$ is expressed as

$$k_n(\omega) = \beta_n(\omega) - j\alpha_n(\omega) \quad (9)$$

where $\alpha_n(\omega)$ and $\beta_n(\omega)$ are defined as

$$\alpha_n(\omega) = \omega\sqrt{\mu\epsilon_n}\left[\frac{1}{2}\sqrt{1 + \frac{\sigma_n^2}{\omega^2\epsilon_n^2}} - \frac{1}{2}\right]^{\frac{1}{2}} \quad (10)$$

$$\beta_n(\omega) = \omega\sqrt{\mu\epsilon_n}\left[\frac{1}{2}\sqrt{1 + \frac{\sigma_n^2}{\omega^2\epsilon_n^2}} + \frac{1}{2}\right]^{\frac{1}{2}}. \quad (11)$$

Here, ϵ_n and σ_n are the relative permittivity and conductivity, respectively, of ablated tissues at the nth snapshot, and ϵ_0 and σ_0 are those of preablated tissues. Organizing (7) and (8), the signal at the nth snapshot from ablated tissues can be approximated as

$$\begin{aligned} S_n(\boldsymbol{r}_\mathrm{C}, \omega; R^{\mathrm{AB}}) &= \frac{G(\|\boldsymbol{r}_\mathrm{B} - \boldsymbol{r}_\mathrm{A}\|; k_n(\omega))}{G(\|\boldsymbol{r}_\mathrm{B} - \boldsymbol{r}_\mathrm{A}\|; k_0(\omega))} S_0(\boldsymbol{r}_\mathrm{C}, \omega; R^{\mathrm{AB}}) \\ &\simeq S_0(\boldsymbol{r}_\mathrm{C}, \omega; R^{\mathrm{AB}}) \cdot e^{j(k_n(\omega) - k_0(\omega))R^{\mathrm{AB}}}. \end{aligned} \quad (12)$$

Finally, the distance from the source to the ablation boundary at the nth moment, $\hat{R}_n^{\mathrm{AB}}$, is calculated as

$$\hat{R}_n^{\mathrm{AB}} = \arg\min_{R^{\mathrm{AB}}} \int \left|S_n(\boldsymbol{r}_\mathrm{C}, \omega; R^{\mathrm{AB}}) - S_n^{\mathrm{obs}}(\boldsymbol{r}_\mathrm{C}, \omega)\right|^2 d\omega \quad (13)$$

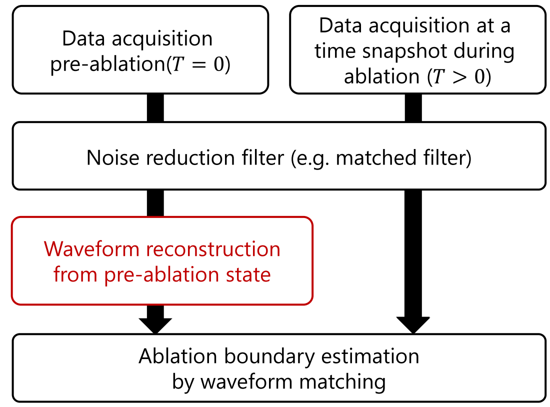

Fig. 2. Procedure of the proposed algorithm. Red box denotes the difference part from the TDOA-based method.

where $S_n^{\mathrm{obs}}(\boldsymbol{r}_\mathrm{C}, \omega)$ denotes the observed signal in the angular-frequency domain at the nth snapshot. Finally, the boundary point of the ablation zone is obtained as $\boldsymbol{r}_\mathrm{B} = \hat{R}^{\mathrm{AB}}\boldsymbol{u} + \boldsymbol{r}_\mathrm{A}$, where $\boldsymbol{u}$ denotes a unit vector pointing from $\boldsymbol{r}_\mathrm{A}$ to $\boldsymbol{r}_\mathrm{C}$.

2) Procedure: The procedure for the proposed method is summarized as follows.

Step 1: The received signals are recorded at $T = 0$ (before the ablation begins) and at the nth temporal snapshot during the ablation.

Step 2: A noise reduction filter (e.g., matched filter) is applied to both observed signals.

Step 3: The waveform in the nth snapshot in the ablation state is derived in (12).

Step 4: $\hat{R}_n^{\mathrm{AB}}$ is determined in (13), and the ablation boundary point $\boldsymbol{r}_\mathrm{B}$ is determined in (5).

Fig. 2 shows the flowchart of the proposed method. This method maintains the advantages described above, in that it only requires the ratio of the dielectric constants and the conductivity in ablated tissues to be known beforehand. In most clinical applications, the source is located inside the malignant tissue, and databases of the complex permittivity of various malignant tissues are available in the literature [11]. It should also be noted that the proposed method (or the TDOA method) does not use a specific dispersive model (e.g., a single-pole Debye) but simply determines the distance from the source to the ablation boundary as $R_A B$ for each direction, using the impact only for the relative permittivity ϵ_n and the conductivity σ_n between preablation and during ablation at the specific frequency. In other words, the nondispersive model is used in this method.

IV. 2-D Numerical Simulation

A. Breast Phantom and Measurement Array

We used an FDTD numerical simulation to assess the imaging performance of each method, using in-house University of Wisconsin-Madison codes. In the simulation, two realistic computational phantoms of breasts derived from MRI data from healthy women were used [13]: a Class 3 "heterogeneously dense" phantom (ID number 062204), and a Class 4 "very dense" (ID number 012304) phantom, data

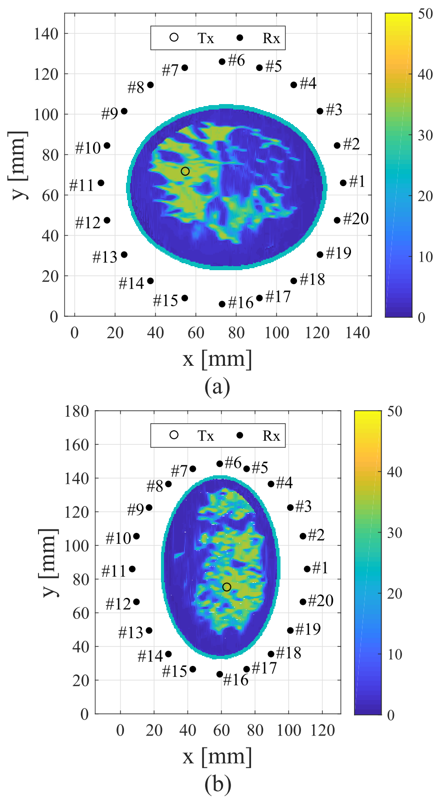

Fig. 3. 2-D numerical breast phantom at preablation state. The colorbar displays the Debye parameter, $\Delta\varepsilon$. (a) Class 3 (heterogeneously dense) breast phantom. (b) Class 4 (extremely dense) breast phantom.

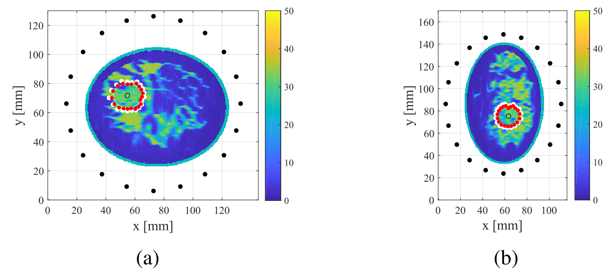

Fig. 4. Estimated boundaries of the elliptical ablation zone by each method. White solid circles denote the estimated points by the TDOA method. Red solid circles denote the estimated points by the proposed method. The colorbar displays the Debye parameter, $\Delta\varepsilon$. (a) Class 3. (b) Class 4.

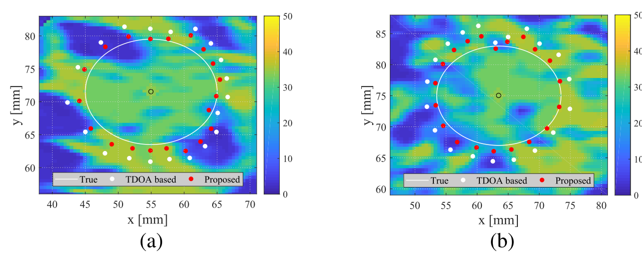

Fig. 5. Enlarged views around the ablation zones of Fig. 4. White solid circles denote the estimated points by the TDOA method. Red solid circles denote the estimated points by the proposed method. The colorbar displays the Debye parameter, $\Delta\varepsilon$. (a) Class 3. (b) Class 4.

for each of which are available online [14]. The frequency-dependent complex permittivities for skin and breast tissues in the phantoms are also modeled by a single-pole Debye models $\bar{\epsilon}(\omega) = \epsilon_\infty + (\epsilon_s - \epsilon_\infty)/1 + j\omega\tau_0 + (\sigma/j\omega\epsilon_0)$ over the frequency range from 0.1 to 5.0 GHz, as in [15]. Fig. 3 shows the maps of the Debye parameter $\Delta\epsilon$ of the Class 3 and Class 4 phantoms. The transmission source is located inside the fibroglandular tissue. Here, we consider that the ablation zone is predominated by the glandular tissue in most cases, because the cancer tissue is usually distributed within the glandular area, and the adipose area is much less than the glandular area in the ablation zone. Then, the average relative permittivity and conductivity of preablated tissue surrounding the source are $\epsilon_0^{\mathrm{AB}} = 42$ and $\sigma_0^{\mathrm{AB}} = 0.633$ S/m, respectively, each of which corresponds to the median value for healthy fibroglandular tissues at $f_0 = 2.45$ GHz. We also locate the tumor around the source, which has a circular shape with 2 mm radius and has the Debye parameter as $(\epsilon_\infty, \Delta\epsilon, \sigma) = (58.0, 20.0, 0.8\ \mathrm{S/m})$. The 20 simulated receiving antennas are located in a ring outside the breast (immersed in air) with equal spacing. The transmitted signal is a Gaussian modulated pulse, with 2.45 GHz as its central frequency and 1.9 GHz at the full bandwidth of 3 dB. The cell size in the FDTD computational domain is 0.5 mm. The in-house University of Wisconsin–Madison FDTD code that assumes the single-pole Debye model is used to generate the data. In other words, the effects of both dispersion and the changes occurring in the surrounding medium are considered. A noiseless case is assumed in order to assess the systematic error caused by the waveform mismatching. All the Debye parameters uniformly decrease in the ablated tissue, that is, the dielectric maps inside or outside the ablation zone are still heterogeneous, and the ratios of decrease from a nonablated state for relative permittivity and conductivity are defined as ξ_ϵ and ξ_σ, respectively. This range of effects has been observed in ablations of bovine liver tissues [5] and human mastectomy specimens [6].

B. Imaging and Waveform Reconstruction Results

For a representative case of ablation treatment, we first tested a simulation in which the impact of the ablation is a uniform 10% drop in all Debye parameters within the ablation zone ($\xi_\epsilon = \xi_\sigma = 0.9$) Thus, the dielectric properties in the ablated region are also heterogeneous. This degree of reduction in dielectric properties has been measured in bovine liver tissues that been ablated to 90 °C [5]. The ablation zone in this test is modeled as an ellipse that spans 20 mm along the x-axis and 16 mm along the y-axis at the particular moment when the "measured" signals are recorded. Fig. 4 shows the results from each algorithm for each of the phantoms in this case of ablation having a relatively minor effect on the tissue. Fig. 5 also denotes the enlarged view of Fig. 4, focusing on the ablation area to make the results clearer. These results show that the proposed method locates the boundary of the ablation zone more accurately than the TDOA method. We consider that the proposed method more accurately estimates the distance R_{AB}, as this method corrects for errors that appear in the waveform with the TDOA method. Note that both the TDOA-based imaging and the proposed algorithms assume that an entire

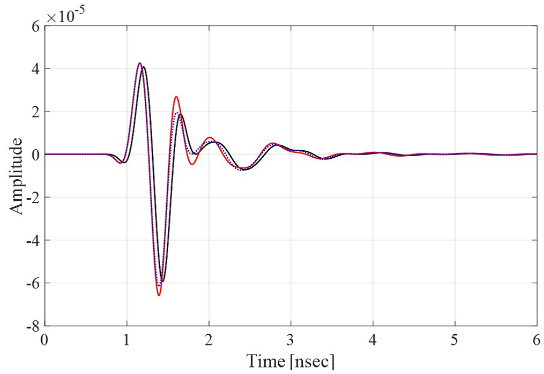

Fig. 6. Example of received signals of preablation (black solid line) and during (red solid line) ablation states at the 15 antennas in Fig. 3(a) at the case of ($\xi_\epsilon = \xi_\sigma = 0.9$) of the Class 3 phantom and waveform reconstruction result (blue dotted line) by the proposed method.

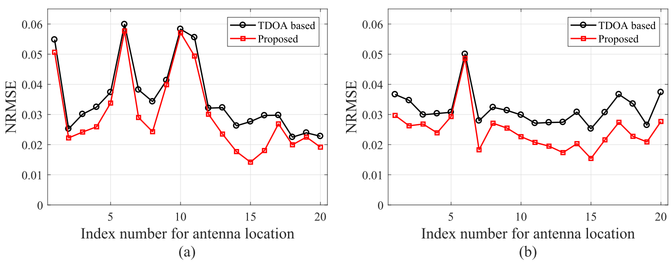

Fig. 7. NRMSE for waveform reconstruction at different antenna location. (The number of index is denoted as in Fig. 3.) (a) Class 3. (b) Class 4.

ablation zone has the homogeneous dielectric map (the same level of ablated tissue and dehydration) for the calculation of the ablation boundary, that is, ϵ_{AB}^0 and σ_{AB}^0 are constant in the entire ablation zone. Although the reconstruction errors shown in Fig. 5 are caused by the heterogeneity of the outside and inside the ablation zone, the proposed method achieves the reconstruction accuracy within 2 mm in the median.

Fig. 6 shows an example of the signal received in states before and during ablation and the waveform reconstructed by the proposed method, in the above case. This figure shows that the waveform received in the state during ablation is slightly deformed from that obtained in the preablation state; this deformation affects the TDOA errors, because the TDOA assumes that the waveforms are identical between the states before and during ablation. Although the TDOA errors are at the same level, as in the higher-impact case, the error denoting $\Delta\tau/(1-\sqrt{\xi})$ becomes larger. In contrast, the waveform comparison in Fig. 6 demonstrates that the proposed algorithm could reconstruct the waveform by compensating for not only the time shift but also the frequency characteristic using the impact of ablation for the conductivity drop, which enhances the accuracy in the estimation of $\hat{R}_n^{\mathrm{AB}}$.

In order to verify the above results, we introduced an error analysis method for use with the waveform reconstruction technique. The normalized root mean square error (NRMSE) is written as

$$\mathrm{NRMSE}_n = \sqrt{\frac{\int_0^T \left|\hat{s}_n(t) - s_n^{\mathrm{obs}}(t)\right|^2 dt}{\int_0^T \left|s_n^{\mathrm{obs}}(t)\right|^2 dt}} \tag{14}$$

where $\hat{s}_n(t)$ denotes the signal reconstructed by either method, where the time shift of $\hat{s}_n(t)$ of the TDOA-based method is compensated for using the time delay $\Delta\tau$ calculated in (6). Fig. 7 shows the NRMSE for each receiving antenna for both phantoms. These results indicate that the proposed method reconstructs waveforms more accurately than the TDOA-based method does. Accurate waveform reconstruction enhances the accuracy of estimating R_{AB}, which results in more accurate images. Note that the average calculation times are 0.1 s with the TDOA-based method and 0.3 s with the proposed method, using an Intel Xeon CPU E5-1620 v2 3.7 GHz, with 16 GB RAM. Both methods, therefore, enable real-time monitoring in tissues whose dielectric properties are strongly affected by ablation. It is also one of the most distinguished advantages of the methods, compared with the inverse scattering algorithm.

C. Statistical Results for Different Types of Ablations and Additive Noises

In order to investigate the range of applications for the proposed method, we next consider a range of different degrees of ablation causing the same levels of reduction in both relative permittivity and conductivity. Here, if $\xi_\epsilon = \xi_\sigma = x$ holds, the simplified notation $\xi = x$ is introduced as the following description. A noiseless case is also assumed here. In addition, to demonstrate the effectiveness of the proposed method in terms of statistical view point, 100 different patterns of the ablation-zone center for each impact are investigated in the Class 3 and Class 4 phantoms. The dimensions of the ablation are fixed for these tests and are the same as in Fig. 5. For these tests, we define the reconstruction error for a specific estimated boundary point, $\boldsymbol{r}_{\mathrm{B}}$, as the shortest distance from that estimated boundary point to the actual boundary. Fig. 8 shows box plots of the median values of the estimation errors delivered by the TDOA-based and the proposed methods, respectively. The lower and upper bounds of the boxes span the interquartile range (IQR) and the lower and upper whiskers denote the standard deviation. These results demonstrate that the proposed method enhances the medians and IQRs for all ablation types. The difference is remarkable, particularly in the case of ξ =0.9 [i.e., $(\xi_\epsilon, \xi_\sigma) = (0.9, 0.9)$], with which the TDOA-based method is significantly inaccurate. This is because the relatively small decrease in the dielectric constant leads to a smaller time shift in the forward-scattered signal $\Delta\tau$. When the imaging algorithm has only TDOA values to work with, its sensitivity to this error in $\Delta\tau$ is quite severe. The proposed method can enhance the accuracy of $\Delta\tau$ estimations, on the other hand, by compensating for the waveform deformation caused by the drop in conductivity.

Next, in order to investigate the sensitivity to additional noise, white Gaussian noise is added to each recorded electric field. The signal-to-noise ratio (SNR) for this simulation is defined as the ratio of the maximum power of received signals to the power of noise in the time domain. We tested a representative case with an SNR of 20 dB. A matched filter was applied to the received simulated signals to reduce noise. Fig. 9 shows box plots of the median values of the estimation errors delivered by the TDOA-based and the proposed methods, respectively. This figure also demonstrates that the proposed

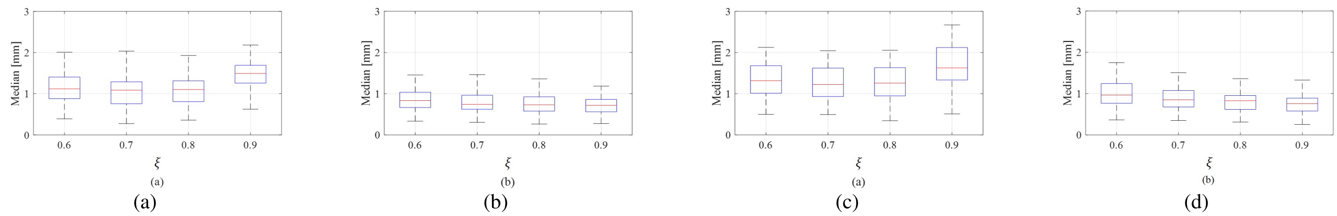

Fig. 8. Box plots of median errors in ablation zone boundary estimation as a function of $\xi(=\xi_\epsilon=\xi_\sigma)$ at each Class phantom on noiseless situation, where 100 different locations of ablation centers with the same dimension are investigated. (a) Class 3 (TDOA). (b) Class 3 (proposed). (c) Class 4 (TDOA). (d) Class 4 (proposed).

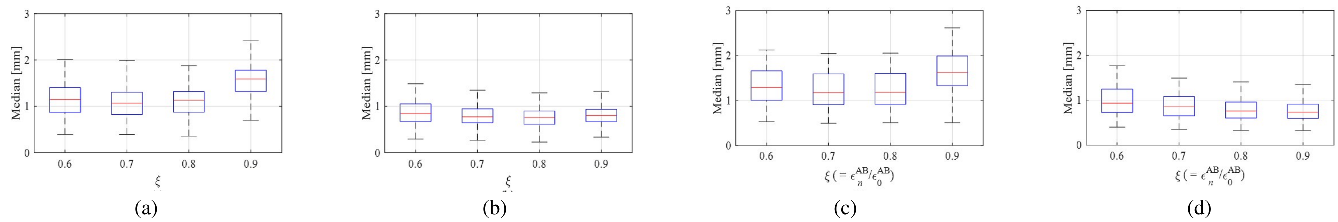

Fig. 9. Box plots of median errors in ablation zone boundary estimation as a function of $\xi(=\xi_\epsilon=\xi_\sigma)$ at each Class phantom at the 20 dB SNR situation, where 100 different locations of ablation centers with the same dimension are investigated. (a) Class 3 (TDOA). (b) Class 3 (proposed). (c) Class 4 (TDOA). (d) Class 4 (proposed).

method attains more accurate ablation boundary points, especially for higher ξ case, and the additional noise does not markedly affect the results in either the TDOA or the proposed method, because the either method adopts the preprocessing filter as the matched filter, which is the most robust to the added noise.

TABLE I

RMSE AND MEDIAN ERRORS IN ESTIMATING THE BLURRED BOUNDARY CASES

	TDOA		Proposed	
	RMSE	Median	RMSE	Median
Case 1	1.79 mm	1.81 mm	1.35 mm	1.39 mm
Case 2	2.42 mm	2.40 mm	1.22 mm	1.14 mm

D. Results in Blurred Ablation Boundary Case

The TDOA and the proposed methods are based on the assumption that the ablation zone has a homogeneous change from the preablation state; however, this is not true for the actual ablation zone. To assess the limitation of the proposed method, we tested the case, wherein the ablation boundary is not clear but gradually changes from the center of the ablation probe, in terms of the Debye parameters. A number of reports [5], [6], [9] demonstrated that the ablation area gradually changes around the ablation boundary. We tested two different impact cases, Case 1 is a large range case ($0.6 \leq \xi, \leq 1$), and Case 2 is a small range case ($0.9 \leq \xi, \leq 1$). Fig. 10 shows the estimation results of the ablation boundary for the TDOA-based method and the proposed method for both cases. In order to show the quantitative analysis for the estimated boundary points, we defined the reconstruction error as the shortest distance from that estimated boundary point to the actual boundary, which has the intermediate change of ξ, namely, the boundary denoting $\xi = 0.8$ for Case 1 and the boundary denoting $\xi = 0.95$ for Case 2. The error analyses for each case of each method are summarized in Table I. In Case 1, each method maintains a certain level of accuracy for the estimated boundary points. However, in Case 2, the TDOA-based method suffers from a degradation of accuracy, although the proposed method maintains the accuracy at the same level as in Case 1, demonstrating that the proposed method is robust to a smaller impact of ablation.

E. Sensitivity to the Impact Parameters of Ablation of ξ_ϵ and ξ_σ

Note that, we need to consider the impact of a mismatch between the actual dielectric constant and conductivity of the target tissue before ablation in the TDOA-based and the proposed methods. Such a mismatch would arise owing to any patient-to-patient variability in the dielectric properties of the target tissue. However, in the literature [11], the above sensitivity in the TDOA-based method is demonstrated, as to the mismatch of ϵ_0, and the possible factors causing such sensitivity are discussed. Those discussions are almost common in the proposed method, because the mismatch of ϵ_0 and σ_0 possibly degrades the performance, but the error level is relatively similar to the results of the TDOA-based method.

To avoid duplicating analyses reported in the literature [11], this article now focuses on the sensitivity of mismatch for the impact parameter as ξ_ϵ and ξ_σ for the estimated ablation boundary points for the TDOA-based and the proposed methods as follows. Here, we assume the Class 3 phantom with the same observation and probe model as in Fig. 3(a). We investigated the simulations, in which the two types of impact of ablation are a uniform 10% [namely, $(\xi_\epsilon, \xi_\sigma) = (0.9, 0.9)$] and 40% $(\xi_\epsilon, \xi_\sigma) = (0.6, 0.6)$. A noiseless situation is assumed, for simplicity. Fig. 11 shows the differences in median errors of the estimated boundary points, where the reference of median errors is set as that obtained using the actual ξ_ϵ and ξ_σ. It is natural that the TDOA-based method has

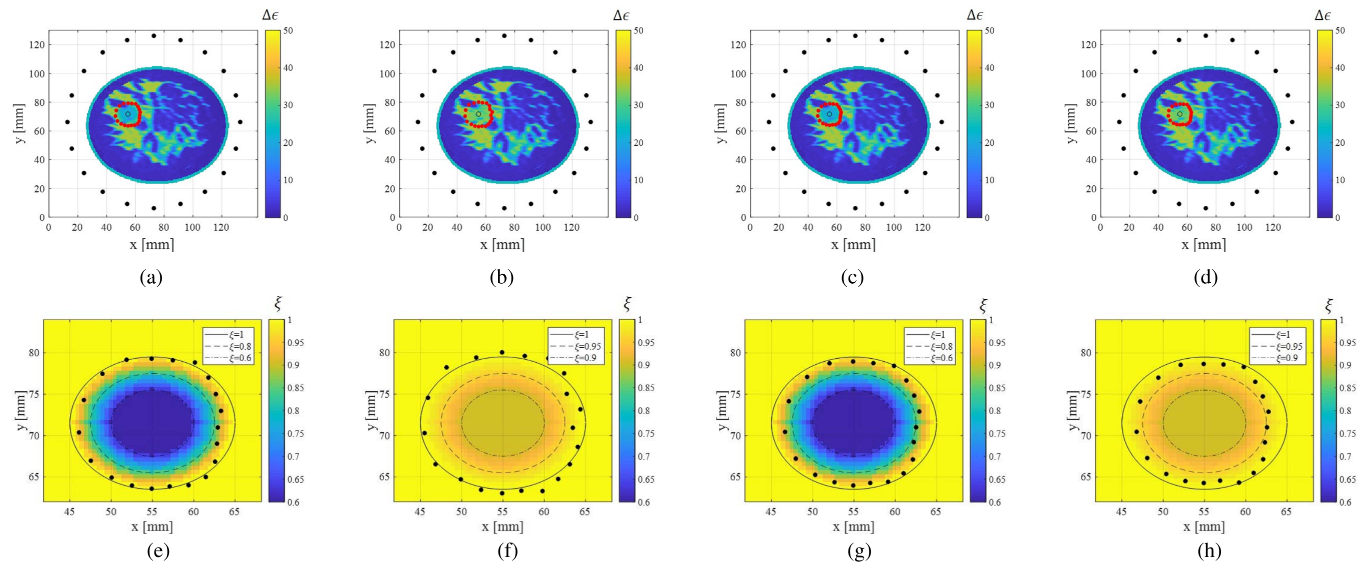

Fig. 10. (a) and (b) Estimated result for blurred ablation boundary case by the TDOA-based method at each case, where the color shows $\Delta\epsilon$. (c) and (d) Estimated result for blurred ablation boundary case by the proposed method at each case, where the color shows $\Delta\epsilon$. (e) and (f) Enlarged views of Fig. 10 (a) and (b), respectively, by the TDOA-based method, where the color shows ξ. (g) and (h) Enlarged view of Fig. 10 (c) and (d), respectively, by the proposed method, where the color shows ξ. (a) Case 1 (TDOA). (b) Case 2 (TDOA). (c) Case 1 (proposed). (d) Case 2 (proposed). (e) Case 1 (TDOA). (f) Case 2 (TDOA). (g) Case 1 (proposed). (h) Case 2 (proposed).

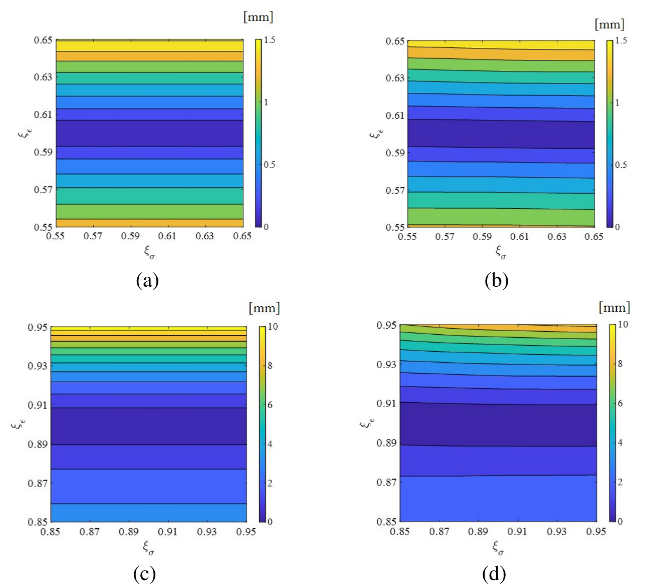

Fig. 11. Median error distributions, when the actual parameters are set as $(\xi_\epsilon, \xi_\sigma) = (0.6, 0.6)$ in (a) and (b), and $(\xi_\epsilon, \xi_\sigma) = (0.9, 0.9)$ in (c) and (d). (a) TDOA. (b) Proposed. (c) TDOA. (d) Proposed.

a sensitivity only for ξ_ϵ, because it does not employ the impact of conductivity in the estimation. While the proposed method has a sensitivity to ξ_σ, ξ_σ has much smaller impact than ξ_ϵ, which is at almost the same level as that in the TDOA-based method. This is considered to be because the dominant cause of the boundary reconstruction may be the error of the time delay, namely, TDOA. However, the small errors of waveform distortion by the error of ξ_σ affect the median or root mean square error (RMSE) of the boundary estimation, especially for a lower impact of ablation.

F. Discussion Assuming a Realistic Scenario

This section presents a discussion in the context of the actual clinical scenario.

1) Limited Aperture Scenario: In the measurement setup described in the previous simulation model, the receiving antennas enclose the region to be imaged. However, that is not necessarily viable in various clinical ablation scenarios (e.g., liver and kidney). Note that because the proposed method (also the TDOA method) is not based on the inverse-problem solution, it does not experience typical problems such as ill-posedness or ambiguity due to a limited number of data. In other words, the estimation accuracy for each ablation boundary received by other receivers. Thus, the proposed method can determine the ablation boundary point even if there is only one sensor outside the breast. The number of receivers has a direct effect on the number of ablation boundary points, and if there are only a few ablation boundary points (e.g., two or three), then naturally the dimension of the ablation zone is estimated poorly. Consequently, the intrinsic problem with our method is that if a limited number of limited directional data are available, then the reconstruction area of the ablation boundary is also limited, which is simply a geometrical limitation.

2) Coupling Medium: In a realistic scenario, there is an option to fill the coupling medium (e.g., oil) into the surrounding area of the breast. With a coupling medium in place, the internal reflection from the skin surface is suppressed considerably, which is more advantageous for our method because now larger responses from the source are available, thereby enhancing the S/N.

3) Case for Larger Ablation Zone: Some previous studies have shown that the actual ablation zone is larger than that assumed in the present numerical tests, namely an ellipsoid with a diameter of approximately 20 mm. Scapaticci *et al.* [16] assumes an ellipsoidal ablation zone with a diameter of 2 cm, but [9] assumes larger dimensions, such as a 40 mm ping-pong ball, and also [17] the following one assumes a lesion with dimensions of around 5.6 × 3.7 cm. The dimension of the real ablation assuming the clinical scenario, also ranges from

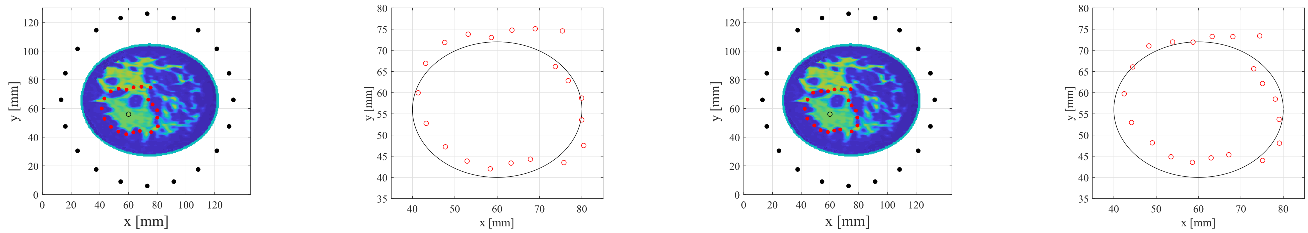

(a) (b) (c) (d)

Fig. 12. Estimated boundaries of larger ablation zone by each method. Red solid circles denote the estimated points by each method. The colorbar displays the Debye parameter, $\Delta\varepsilon$. (b) and (d) Enlarged view for each estimation boundary, where black solid curve shows the actual ablation zone boundary. (a) TDOA. (b) Proposed. (c) TDOA. (d) Proposed.

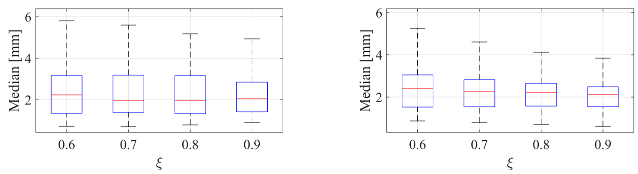

(a) (b)

Fig. 13. Box plots of median errors in ablation zone boundary estimation as a function of $\xi(=\xi_\epsilon = \xi_\sigma)$ at each Class phantom at noise-free situation, where 90 different locations of ablation centers with the same dimension are investigated. (a) TDOA. (b) Proposed.

3 to 3.5 cm diameter [18], [19]. Consequently, we investigate the case for a larger ablation zone as follows. Fig. 12 shows the results obtained using the TDOA method and the proposed method, where the ablation zone is an ellipse with a major radius of 20 mm and a minor radius of 16 mm. Here, we assume $\xi = 0.9$. As shown in Fig. 12, the errors are significant and are greater than in the cases with smaller dimensions. These errors are considered to be caused by the simplified propagation model in the TDOA method and the proposed method, namely the straight-line propagation or the homogeneous and nondispersive property of the ablation zone. The RMSE and median error for the ablation boundary points are 2.77 and 2.67 mm, respectively, for the TDOA method and 2.82 and 1.91 mm, respectively, for the proposed method. Fig. 13 shows box plots for the median error with each method on changing ξ. Although there is a slight improvement with the proposed method in terms of the median error at higher ξ, it is less distinct compared with that obtained in cases with smaller dimensions. Note that our proposed method is focused on monitoring the evolution of the ablation zone, where the initial state of ablation with smaller size or a lower impact of dielectric change should also be assessed at each elapsed time. Although the proposed method has a clear advantage only at the beginning of ablation, it is promising for monitoring safety in the early stage of ablation.

4) Sensitivity to Movement During Ablation: The movement of the patient due to breathing and heartbeat affects the estimation results of both the TDOA method and the proposed method. This sensitivity of each method is investigated as follows. We assume the same observation model as that of the Class phantom in Fig. 3 at the preablation state. During ablation, the entire breast is slightly shifted along the y-axis, which is defined as ΔY. In the reconstruction using each method, the geometrical conditions of the source and receivers should be used as the preablation state because the small fluctuation of the breast location is hardly measured at each elapsed time during ablation. Fig. 14 shows the reconstruction results for each method when we investigate the cases of $\Delta Y = 1.0$, which is almost the average displacement level by a respiration. In comparison with the results in Fig. 4 (i.e., no motion during ablation), there are some offset errors in each motion case, but these are of the same level for both values of ΔY. The RMSE and median error for the ablation boundary points are 4.11 and 3.17 mm, respectively, for the TDOA method and 3.42 and 2.65 mm, respectively, for the proposed method. However, in the case for larger movement of breast during ablation, we need to compensate those errors to attain a sufficient accuracy, and a real-time radar measurement for breast surface would be a promising option for the above correction.

G. Comparison Study for 2-D Distorted Born Iterative Method (DBIM)-Based Inverse Scattering Method

To clarify the effectiveness of the proposed method, comparing the typical inverse scattering analysis, this section introduces the imaging example by the DBIM, which has been demonstrated in the number of breast media reconstruction such as cancer detection [20], [21]. The DBIM is one of the promising algorithm, which reconstructs the highly heterogeneous and dispersive media, using the iterative procedure for forward and inverse solvers. Here, we introduce the example of the DBIM in the Class 3 case. The observation model is the 2-D model, which is the same as in Section IV. For simplicity, it assumes that the initial maps of the Debye parameters are given as that of the preablation state shown as in Fig. 3(a). Here, to accelerate the calculation speed, the cell size of the FDTD and unknowns of the DBIM is set to 2 mm. The conjugate gradient for least-squares (CGLS) method under l_2 norm regularization is used to update the DBIM with 20 being the maximum number of iterations with convergence check, which has been empirically determined by investigating several cases. The forward solver is also given by the 2-D FDTD method, which is the same for the data generation. Fig. 15 shows the reconstruction results of the DBIM, that is, the difference between the preablation and during ablation states at the case of $\xi_\epsilon = \xi_\sigma = 0.9$, where the number of iterations is 100. The RMSEs between the actual and estimated difference map for each Debye parameter are 0.285 for ϵ_∞ (17.7% relative error), 0.540 for $\Delta\epsilon$ (19.9%

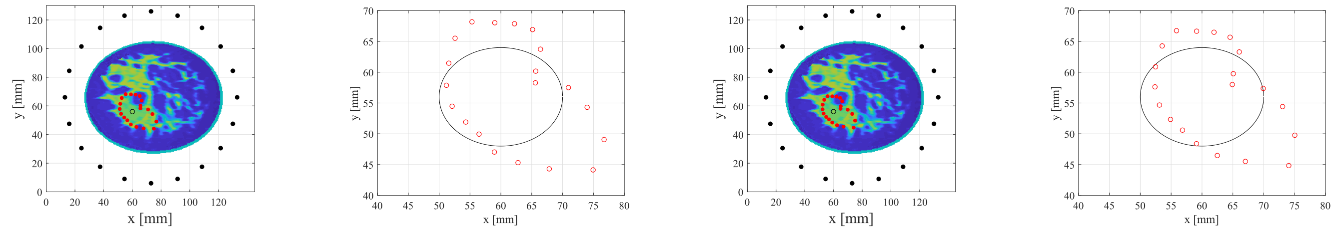

(a) (b) (c) (d)

Fig. 14. Estimated boundaries by each method, where the location of the breast is slightly shifted ($\Delta Y = 1$ mm) at the during ablation state. Red solid circles denote the estimated points by each method. (a) TDOA. (b) TDOA. (c) Proposed. (d) Proposed.

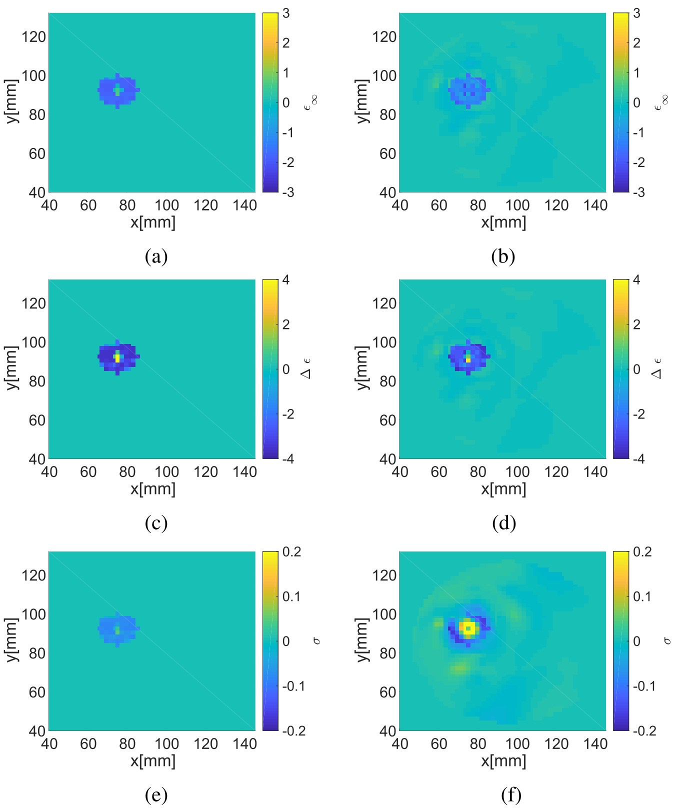

Fig. 15. Results of DBIM-based ablation zone reconstruction in the case of $(\xi_\epsilon, \xi_\sigma) = (0.9, 0.9)$. (a), (c), and (e) Actual difference between preablation and during ablation maps. (b), (d), and (f) Estimated map by the DBIM with 100 iterations. (a) Actual difference of ϵ_∞. (b) Estimated difference of ϵ_∞. (c) Actual difference of $\Delta\epsilon$. (d) Estimated difference of $\Delta\epsilon$. (e) Actual difference of σ. (f) Estimated difference of σ.

relative error), and 0.029 S/m for σ (44.1% relative error), where the average values of the actual difference map are 1.613 for ϵ_∞, 2.714 for $\Delta\epsilon$, and 0.0068 S/m for σ. As shown in this figure and the above quantitative result, the DBIM could offer the significant information about the area and impact of the ablation zone without using the ablation impact parameter of ξ_ϵ and ξ_σ, which is the advantage of the DBIM method from the proposed method. However, the accuracy of the DBIM largely depends on the initial estimate, and in this case, it is given the accurate map of preablation state, which is hardly obtained in the realistic scenario. In addition, the calculation time for the reconstruction is over 30 min using an Intel Xeon CPU E5-1620 v2 3.7 GHz, with 16 GB RAM, and this is a severe disadvantage from the proposed method, in terms of computational time, in particular for the 3-D

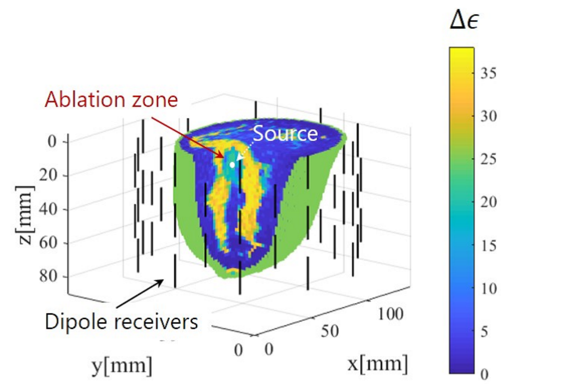

Fig. 16. 3-D numerical breast phantom (Class 3) and configuration, where the MWA probe is set to the short electric dipole. The colorbar displays the Debye parameter, $\Delta\epsilon$. The red circles denote the locations of the 50 electrically short receiving dipole antennae (black solid line) located on elliptical rings surrounding the breast phantom.

extension. However, we consider that the appropriate hybrid of the proposed method and the inverse scattering algorithm could offer more effective imaging algorithm for the real-time, accurate, and less prior knowledge imaging.

V. 3-D Numerical Test With Realistic Phantom

A. Numerical Setting

In this section, we present the performance test of each method, based on the 3-D numerical simulation, using the FDTD calculation. Fig. 16 shows the observation model in this 3-D test, where the Debye parameter, $\Delta\epsilon$, of the Class 3 phantom is presented. The 3-D FDTD simulations, considering the dispersive model, were conducted using commercial software, namely, the XFDTD Bio-Pro, a product by Remcom Inc., where the single-pole Debye dispersion model is implemented for data generation. The 3-D computational domain is composed of 0.5 mm cubic grid cells, but the phantom is resampled as 2 mm cells owing to the limitations of the computer memory. The transmitted signal is a Gaussian modulated pulse, with 2.45 GHz as the central frequency and a 1.9 GHz as that at full 3 dB bandwidth. The receiving antenna array surrounding the breast phantom consists of 50 electrically short dipoles, where each dipole arm is 10 mm in length and the feed gap is 0.5 mm. These receiving antennae are evenly distributed on five elliptical rings of eight antennae each, with adjacent rings rotated by 18° to create a staggered array of antennae in the vertical direction. The five rings are located on the xy planes located at $z = 5$ mm, $z = 20$ mm, $z = 35$ mm, $z = 50$ mm, and $z = 65$ mm. The antennae are used to measure

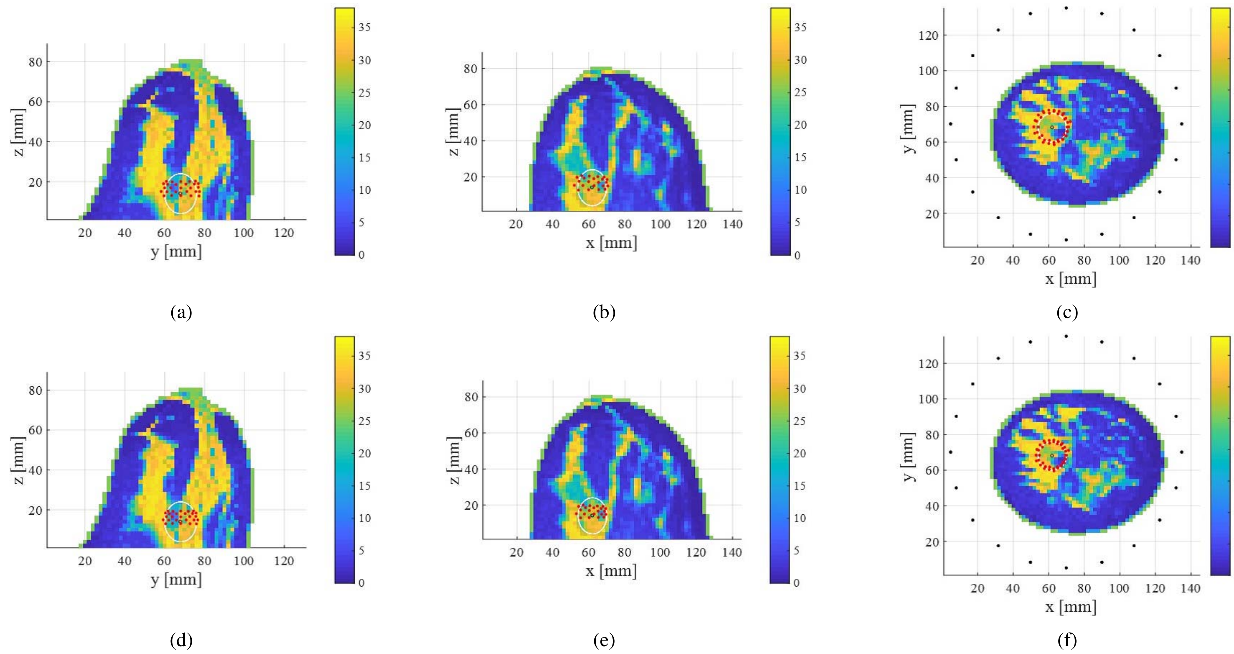

Fig. 17. Estimated boundary points shown by the red circles of the ellipsoidal ablation zone by each method, in the 3-D Class 3 numerical breast phantom at a noiseless case, where the actual ablation boundary is expressed as white solid curves. (a) and (d) x plane projection. (b) and (e) y plane projection. (c) and (f) z plane projection. (a) TDOA $\xi = 0.9$. (b) TDOA $\xi = 0.9$. (c) TDOA $\xi = 0.9$. (d) Proposed $\xi = 0.9$. (e) Proposed $\xi = 0.9$. (f) Proposed $\xi = 0.9$.

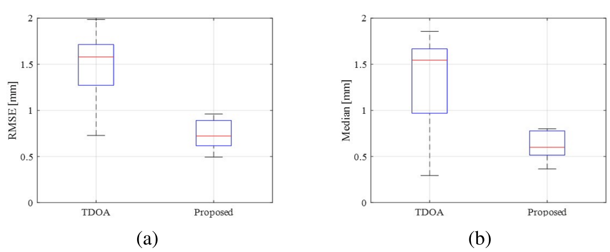

Fig. 18. Box plots of RMSE and median errors in 3-D ablation zone boundary estimation at the case of $(\xi_\epsilon, \xi_\sigma) = (0.9, 0.9)$ on Class 3 phantom on noiseless situation, where ten different locations of ablation centers with the same dimension are investigated. (a) RMSE. (b) Median.

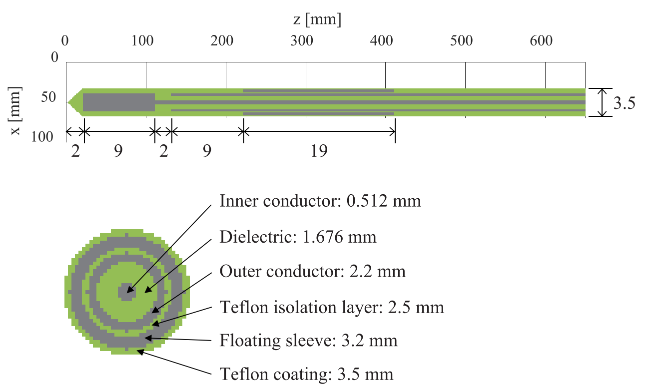

Fig. 19. (a) Design of floating sleeve antenna and (b) its cross section, which is reference by Yang *et al.* [17].

the copolarized electric field component in the feed gap. The time-domain electric fields are recorded at every antenna in the external array. A noiseless situation is assumed to assess the systematic error of the methods.

B. Case in Short Dipole MWA Probe

The transmitting source is an electrically short dipole located within a region of fibroglandular tissues at

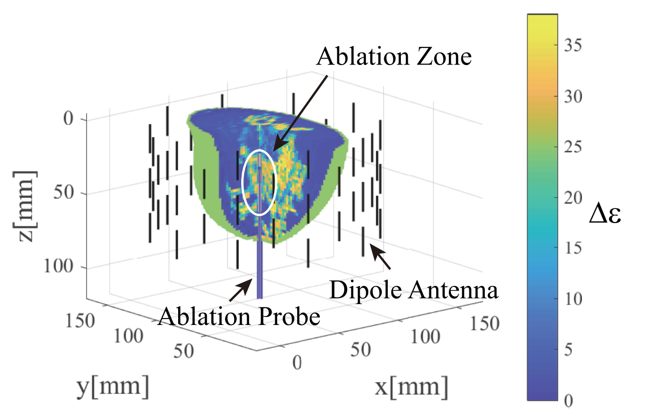

Fig. 20. 3-D numerical breast phantom (Class 4) and configuration, where the MWA probe is set to the coaxial slot antenna. The colorbar displays the Debye parameter, $\Delta\epsilon$. The red circles denote the locations of the 50 electrically short receiving dipole antennas located on elliptical rings surrounding the breast phantom.

$(x, y, z) = (48\ \text{mm}, 75\ \text{mm}, 13\ \text{mm})$. The ablation zone (shown in Fig. 16) is modeled as an ellipsoid with axial radii of 8 mm (x-axis), 8 mm (y-axis), and 10 mm (z-axis). The average relative permittivity and conductivity of preablated tissue surrounding the source are $\epsilon_0^{\mathrm{AB}} = 42$ and $\sigma_0^{\mathrm{AB}} = 0.633$ S/m, respectively, which are the same in the 2-D model. We considered the lower impact case, in which the dielectric properties are reduced by 10% for all Debye parameters, namely, the case of $(\xi_\epsilon, \xi_\sigma) = (0.9, 0.9)$. Fig. 17 shows the estimated boundary points by the TDOA-based method and the proposed method, on each of three orthogonal projection planes. The median of errors is 1.70 mm for the TDOA-based method and 0.66 mm for the proposed method. These data and the above quantitative analyses demonstrate that the proposed method enhances the accuracy of boundary extraction, by considering the conductivity drop, even in the 3-D case, the reason for

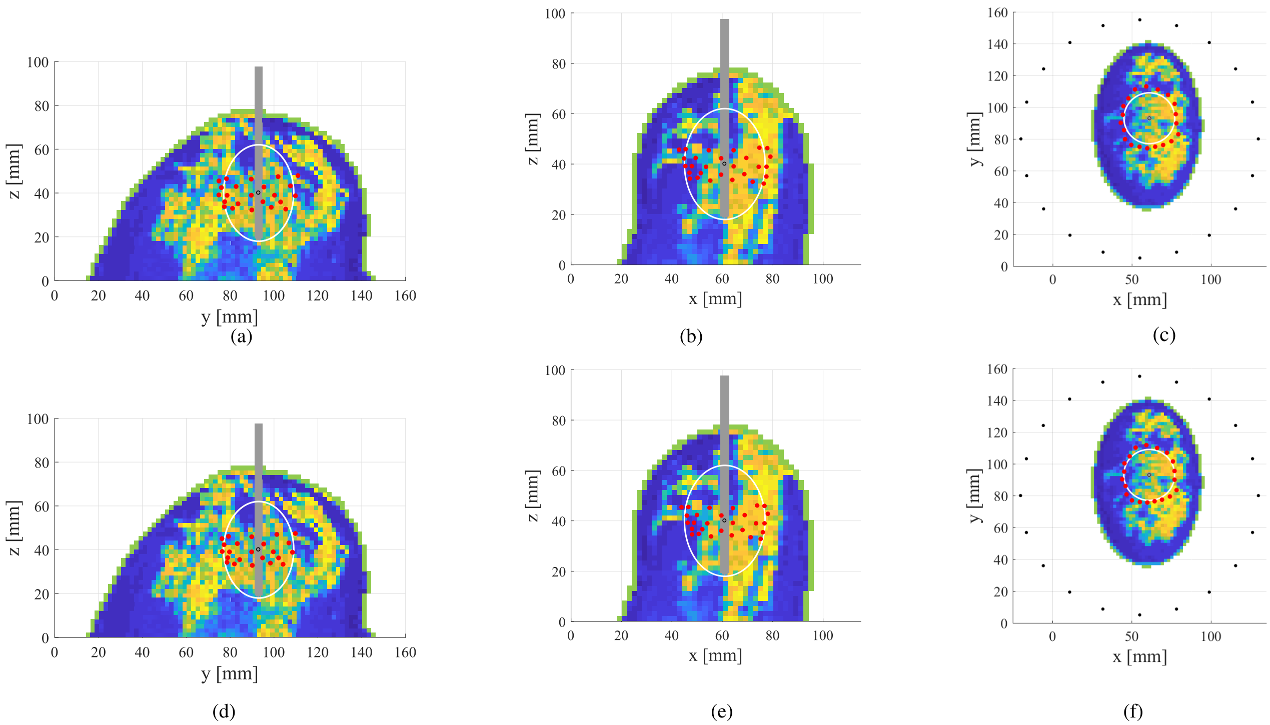

Fig. 21. Estimated boundary points shown by the red circles of the ellipsoidal ablation zone by each method, in the 3-D Class 3 numerical breast phantom at a noiseless case, where the actual ablation boundary is expressed as white solid curves. (a) and (d) x plane projection. (b) and (e) y plane projection. (c) and (f) z plane projection. (a) TDOA $\xi = 0.9$. (b) TDOA $\xi = 0.9$. (c) TDOA $\xi = 0.9$. (d) Proposed $\xi = 0.9$. (e) Proposed $\xi = 0.9$. (f) Proposed $\xi = 0.9$.

which is also the same as that described in the 2-D case. Note that the proposed method (or the TDOA-based method) only exploits the differential information of the received signals between the preablation and during ablation states for each Rx. Mostly, such differential information includes the change in the dielectric property of the area from A to B but not of the area from B to C because the dielectric property of the area from B to C is almost the same during ablation. Small impacts are witnessed in the area from B to C (not in the ablation zone) due to the ablation; however, we consider that the impacts are much less than the impacts in the area from A to B (ablation zone).

For the statistical validation in this case, Fig. 18 shows a box plot of the RMSE and median values of errors, where ten different patterns of the ablation-zone center are simulated in the Class 3. The dimensions of the ablation are fixed for these tests and are the same as in Fig. 16. The lower and upper bounds of the boxes span the IQR and the lower and upper whiskers denote the standard deviation. This figure also shows that the proposed method has an advantage regarding the reconstruction accuracy in the statistical mean. Note that, the clinical reference [22], regarding MWA treatment for a benign breast lesion showed that the mean of its longest diameter is in the range from 5 to 15 mm based on investigating 725 benign breast lesions from 314 women. This article focuses on the real-time monitoring of the time evolution of the ablation zone, in which case, given the aforementioned treatment of benign breast lesions, accuracy of the order of a few millimeters would be significant, especially at the start of ablation with a lower impact of dielectric change (e.g., $\xi = 0.9$). The problem with the conventional TDOA method is that it is highly sensitive to the error of TDOA estimation in the case of lower ablation impact (lower temperature in the ablation zone). In contrast, the proposed method suppresses the relative error of dimension estimation from 10% to 5%, thereby contributing to more-accurate and safer monitoring, especially during the early stage of ablation treatment.

C. Case of Coaxial Slot MWA Probe

This section investigates a case to test the practical applicability of the proposed method, where a coaxial probe is used as the MWA source. Yang *et al.* [18], we adopt a floating sleeve antenna as the coaxial probe for the ablation, which is suitable for achieving a highly localized specific absorption rate pattern. Fig. 19 shows the actual design of the antenna derived from [18]. In this test, the origin of the ablation zone is regarded as the center of the slot area, and the distance estimated as $\hat{R}^{\mathrm{AB}}$ is considered to have an offset of the radius of the probe, namely 1.75 mm. Fig. 20 shows the observation model using the above coaxial probe, assuming the Class 4 "dense" phantom, where the location and dimension of the ablation zone, the impact of ablation [namely the case of $(\xi_\epsilon, \xi_\sigma) = (0.9, 0.9)$], the receivers, and other simulation parameters are the same as those in Section V-B. The radii of the ellipsoidal ablation zone are 16 mm for the x-axis, 16 mm for the y-axis, and 22 mm for the z-axis. Fig. 21 shows the boundary points estimated by the TDOA method and the proposed method on each of three orthogonal projection planes using the coaxial slot probe. The median error is 1.95 mm for the TDOA method and 1.85 mm for the proposed method. Compared with the case of the short dipole source in Section V-B, both methods are inaccurate because volumetric scattering from the coaxial probe interacts with the evolving ablation, which is not considered in the propagation model for the TDOA method and the proposed method. The other cause is considered to be the signal leakage from the insertion point of the coaxial probe, where the electromagnetic wave propagating along the surface of the coaxial probe interferes with the signal propagating into the ablation zone. Actually, the imaging accuracy degrades at the top of the estimation ring, where the distance from the insertion point of the probe is less, and the leakage effect is more dominant in this area. Consequently, these results show that a more appropriate propagation model should be considered in the actual case. However, when dealing with an ablation zone whose diameter exceeds 40 mm, the error level remains within 2 mm.

VI. Conclusion

In this article, we proposed a real-time imaging algorithm based on waveform reconstruction for estimating the dimensions of the ablation zone in the microwave imaging scenario. This algorithm accounts for the impact of the ablated tissue's drop in conductivity, adding to the conventional TDOA-based method's accounting for drops in the relative permittivity. The proposed algorithm compensates for the mismatch between the waveforms of signals before and during the ablation of tissues, which enhances the algorithm's accuracy in estimating the distance from the source antenna to the edge of the ablated zone, especially in the case when the tissue's dielectric properties are less affected by ablation. A 2-D numerical investigation using dispersive FDTD simulations with 100 different samples demonstrated that the proposed algorithm achieves a significantly more accurate boundary estimation for MWA monitoring even in the case where ablation only slightly affects the tissue's dielectric properties. Furthermore, some sensitivity studies for additive noise, blurred boundary, and the mismatch of the impact parameters of ξ_ϵ and ξ_σ have shown that the proposed method has almost the same level of robustness for such fluctuations and mismatches as the TDOA-based method, while maintaining the original advantage of the proposed method.

Finally, 3-D FDTD using realistic breast phantom model has confirmed that the proposed method accurately reconstructs the 3-D ablation boundary, which is more distinct in the lower-impact case. Of course, there are errors due to the frequency dependence of the complex permittivity, and these errors are included in all the results in this article. Nevertheless, our method offers a certain level of accuracy for highly heterogeneous and dispersive media, and we also consider that the results of our method could become an appropriate initial guess for a postimaging algorithm (e.g., inverse scattering) that considers a more accurate propagation model. The proposed algorithm is based on a simple propagation model, namely homogeneous, nondispersive, and straight-line propagation, which is not accurate in a realistic scenario. However, a number of FDTD-based numerical analyses using highly heterogeneous and dispersive breast phantoms showed that our proposed method provides a certain level of accuracy with an extremely low computational cost and without much prior knowledge, which is a significant advantage over other existing methods, particularly the inverse-scattering algorithm. In addition, the comparison study for the DBIM-based ablation zone reconstruction, which is one of the most promising inverse scattering algorithms, has been investigated. While the DBIM method could reconstruct the difference of the dielectric profile with heterogeneous map between preablation and during ablation states, it requires an expensive computational cost. Nonetheless, the hybrid use of our method and inverse scattering scheme would be a promising solution to maintain the reconstruction accuracy, especially in the larger ablation zone, or to accelerate a computational speed, because the rough estimation of the ablation zone by our proposed method could be exploited as an appropriate initial estimate for the inverse scattering, which could accelerate the convergence speed in the iterative procedure and reduce the total computational cost or avoid the local minimum to reconstruct the dielectric profile during ablation. It is our emergent future task to implement the above incorporation algorithm.

Furthermore, it should be also noted that our proposed method (also the TDOA method) does not use *a priori* knowledge that the ablation boundary has a spherical or ellipsoidal shape, but it assumes that the ablation boundary intersects the path A to path C only once. If the above assumption is not guaranteed, it is expected that the proposed method could not maintain the accuracy, naturally. However, a number of literatures [23]–[25] have demonstrated that the ablation zone, especially for bovine liver, usually forms a convex shape, because the energy radiated from the source is transmitted almost omnidirectionally. Note that there are still no reports for the shape of the breast ablation tissue, however, that the above phenomenon should be almost consistent even for the heterogeneous breast media. Then, it is considered that the above limitation of the proposed method would not be fatal for the actual ablation scenario. Finally, both the proposed method and the TDOA method would be inaccurate in cases where the breast tissue undergoes significant morphological changes (e.g., shrinkage) between preablation and during ablation. In particular, shrinkage of all the tissues causes an earlier time of arrival from the source to each receiver, whereupon the algorithm could overestimate the dimension of the ablation zone. The above point has not been addressed in this article, but incorporation with accurate breast surface imaging algorithms (see [26], [27]) is promising for compensating the error caused by the aforementioned morphological changes of the breast. For an actual scenario, a complex-permittivity estimator using the S_{11} parameter, for example, would be a promising means of addressing the interpatient variability of the complex permittivity.

Acknowledgment

The authors thank Prof. S. C. Hagness and the members of the University of Wisconsin Cross-Disciplinary Electromagnetics Laboratory, for the in-house FDTD simulation code.

References

[1] G. Carrafiello *et al.*, "Microwave tumors ablation: Principles, clinical applications and review of preliminary experiences," *Int. J. Surgery*, vol. 6, pp. S65–S69, Dec. 2008.

[2] R. C. G. Martin, C. R. Scoggins, and K. M. Mcmasters, “Safety and efficacy of microwave ablation of hepatic tumors: A prospective review of a 5-year experience,” *Ann. Surg Oncol.*, vol. 17, no. 1, pp. 171–178, Jan. 2010.

[3] L. G. Merckel *et al.*, “MR-guided high-intensity focused ultrasound ablation of breast cancer with a dedicated breast platform,” *Cardiovasc Intervent. Radiol.*, vol. 36, no. 2, pp. 292–301, Apr. 2013.

[4] C. Correa-Gallego, A. M. Karkar, S. Monette, P. C. Ezell, W. R. Jarnagin, and T. P. Kingham, “Intraoperative ultrasound and tissue elastography measurements do not predict the size of hepatic microwave ablations,” *Acad. Radiol.*, vol. 21, no. 1, pp. 72–78, Jan. 2014.

[5] V. Lopresto, R. Pinto, G. A. Lovisolo, and M. Cavagnaro, “Changes in the dielectric properties of ex vivo bovine liver during microwave thermal ablation at 2.45 GHz,” *Phys. Med. Biol.*, vol. 57, no. 8, pp. 2309–2327, 2012.

[6] R. O. Mays, N. Behdad, and S. C. Hagness, “Array sensitivity for model-based microwave breast imaging,” *IEEE Trans. Antennas Propag.*, vol. 65, no. 6, pp. 2958–2965, Jun. 2017.

[7] O. M. Bucci, M. Cavagnaro, L. Crocco, V. Lopresto, and R. Scapaticci, “Microwave ablation monitoring via microwave tomography: A numerical feasibility assessment,” in *Proc. 10th Eur. Conf. Antennas Propag. (EuCAP)*, Apr. 2016, pp. 1–5.

[8] R. Scapaticci, V. Lopresto, R. Pinto, M. Cavagnaro, and L. Crocco, “Monitoring thermal ablation via microwave tomography: An *ex vivo* experimental assessment,” *Diagnostics*, vol. 8, no. 4, p. 81, Dec. 2018.

[9] M. Haynes, J. Stang, and M. Moghaddam, “Real-time microwave imaging of differential temperature for thermal therapy monitoring,” *IEEE Trans. Biomed. Eng.*, vol. 61, no. 6, pp. 1787–1797, Jun. 2014.

[10] G. Chen, J. Stang, M. Haynes, E. Leuthardt, and M. Moghaddam, “Real-time 3D microwave monitoring of interstitial thermal therapy,” *IEEE Trans. Biomed. Eng.*, vol. 65, no. 3, pp. 528–538, Mar., 2018.

[11] S. Kidera, L. M. Neira, B. D. Van Veen, and S. C. Hagness, “TDOA-based microwave imaging algorithm for real-time microwave ablation monitoring,” *Int. J. Microw. Wireless Technol.*, vol. 10, no. 2, pp. 169–178, Mar. 2018.

[12] K. Kanazawa and S. Kidera, “Waveform matching based real-time ablation monitoring for microwave breast cancer ablation,” in *Proc. 12th Eur. Conf. Antennas Propag. (EuCAP)*, 2018.

[13] M. Lazebnik *et al.*, “A large-scale study of the ultrawideband microwave dielectric properties of normal, benign and malignant breast tissues obtained from cancer surgeries,” *Phys. Med. Biol.*, vol. 52, no. 20, pp. 6093–6115, Oct. 2007.

[14] University of Wisconsin Cross-Disciplinary Electromagnetics Laboratory. *Numerical Breast Phantom Repository*. Accessed: Oct. 2, 2017. [Online]. Available: http://uwcem.ece.wisc.edu

[15] L. M. Neira, B. Van Veen, and S. C. Hagness, “Strategies for monitoring microwave ablation of breast tumors using microwave imaging,” in *Proc. IEEE AP-S Symp.*, Jun. 2016, p. 1.

[16] R. Scapaticci, G. G. Bellizzi, M. Cavagnaro, V. Lopresto, and L. Crocco, “Exploiting microwave imaging methods for real-time monitoring of thermal ablation,” *Int. J. Antennas Propag.*, vol. 2017, Nov. 2017, Art. no. 5231065.

[17] D. Yang *et al.*, “A floating sleeve antenna yields localized hepatic microwave ablation,” *IEEE Trans. Biomed. Eng.*, vol. 53, no. 3, pp. 533–537, Mar. 2006.

[18] F. Primavesi *et al.*, “Thermographic real-time-monitoring of surgical radiofrequency and microwave ablation in a perfused porcine liver model,” *Oncol. Lett.*, vol. 15, pp. 2913–2920, Dec. 2017.

[19] M. Meloni *et al.*, “Microwave ablation in primary and secondary liver tumors: Technical and clinical approaches,” *Int. J. Hyperthermia.*, vol. 33, no. 1, pp. 15–24 Feb. 2017.

[20] F. Gao, B. D. Van Veen, and S. C. Hagness, “Sensitivity of the distorted born iterative method to the initial guess in microwave breast imaging,” *IEEE Trans. Antennas Propag.*, vol. 63, no. 8, pp. 3540–3547, Aug. 2015.

[21] L. M. Neira, B. D. Van Veen, and S. C. Hagness, “High-resolution microwave breast imaging using a 3-D inverse scattering algorithm with a variable-strength spatial prior constraint,” *IEEE Trans. Antennas Propag.*, vol. 65, no. 11, pp. 6002–6014, Nov. 2017.

[22] W. Zhang *et al.*, “Clinical application of ultrasound-guided percutaneous microwave ablation for benign breast lesions: A prospective study,” *BMC Cancer*, vol. 19, Apr. 2019, Art. no. 345.

[23] H. Luyen, S. C. Hagness, and N. Behdad, “A balun-free helical antenna for minimally invasive microwave ablation,” *IEEE Trans. Antennas Propag.*, vol. 63, no. 3, pp. 959–965, Mar. 2015.

[24] H. Luyen, F. Gao, S. C. Hagness, and N. Behdad, “Microwave ablation at 10.0 GHz achieves comparable ablation zones to 1.9 GHz in *ex vivo* bovine liver,” *IEEE Trans. Biomed. Eng.*, vol. 61, no. 6, pp. 1702–1710, Jun. 2014.

[25] Y. Lin and P. Liang, “Percutaneous ultrasound-guided microwave ablation of liver metastasis,” in *Microwave Ablation Treatment Solid Tumors*, P. Liang, X. Yu and J. Yu, Eds. Heidelberg, Germany: Springer, 2015, pp. 29–40.

[26] D. Winters, J. Shea, E. Madsen, G. Frank, B. Van Veen, and S. Hagness, “Estimating the breast surface using UWB microwave monostatic backscatter measurements,” *IEEE Trans. Biomed. Eng.*, vol. 55, no. 1, pp. 247–256, Jan. 2008.

[27] K. Noritake and S. Kidera, “Boundary extraction enhanced distorted born iterative method for microwave mammography,” *IEEE Antennas Wireless Propag. Lett.*, vol. 18, no. 4, pp. 776–780, Apr. 2019.

Kazuki Kanazawa received the B.E. degree in electrical, electronics and information engineering from Kanagawa University, Kanagawa, Japan, in 2017 and the M.E. degree in computer and network engineering from the University of Electro-Communications, Tokyo, Japan, in 2019.

He joined Renesas Electronics Corporation, Tokyo, in 2019.

Kazuki Noritake received the B.E. degree in communication engineering and informatics and the M.E. degree in computer and network engineering from the University of Electro-Communications, Tokyo, Japan, in 2017 and 2019, respectively.

He joined KONICA MINOLTA, INC., Tokyo, in 2019. His research interests are signal processing and inverse problem for microwave mammography.

Yuriko Takaishi is currently pursuing the B.E. degree in communication engineering and informatics with the University of Electro-Communications, Tokyo, Japan.

Her research interests are signal processing and inverse scattering analysis for microwave ablation monitoring.

Shouhei Kidera (Member, IEEE) received the B.E. degree in electrical and electronic engineering and M.I. and Ph.D. degrees in informatics from Kyoto University, Kyoto, Japan, in 2003, 2005, and 2007, respectively.

He has been with Graduate School of Informatics and Engineering, University of Electro-Communications, Tokyo, Japan, since 2009, where he is currently an Associate Professor. He stayed at the Cross-Disciplinary Electromagnetics Laboratory, University of Wisconsin–Madison, Madison, WI, USA, as a Visiting Researcher, in 2016. He has been a Principal Investigator of the PRESTO Program of the Japan Science and Technology Agency (JST) for the period of 2017–2021. His current research interest is in advanced radar signal processing or electromagnetic inverse scattering issue for ultrawideband (UWB) 3-D sensor or biomedical applications.

Dr. Kidera is a member of the Institute of Electronics, Information, and Communication Engineers of Japan (IEICE), the Institute of Electrical Engineering of Japan (IEEJ), and the Japan Society of Applied Physics (JSAP). He was a recipient of the 2012 Ando Incentive Prize for the Study of Electronics, the 2013 Young Scientist’s Prize by the Japanese Ministry of Education, Culture, Sports, Science and Technology (MEXT), and the 2014 Funai Achievement Award.